

Selective thermal evolution of native oxide layer in Nb and Nb₃Sn-coated SRF grade Nb: An *in-situ* angular XPS study.

Arely Cano¹, Grigory V. Ereemeev^{1*}, Juan R. Zuazo², Jaeyel Lee¹, Bing Luo³, Martina Martinello^{1,4}, Alexander Romanenko¹, Sam Posen^{1*}

¹Fermi National Accelerator Laboratory, Batavia, Illinois, 60510, USA.

²Spanish CRG beamline at the European Synchrotron Radiation Facility, B.P. 220, F-38043 Grenoble, France

³Characterization Facility, University of Minnesota, 12 Shepherd Labs, 100 Union St. SE, Minneapolis, MN, 55455, USA

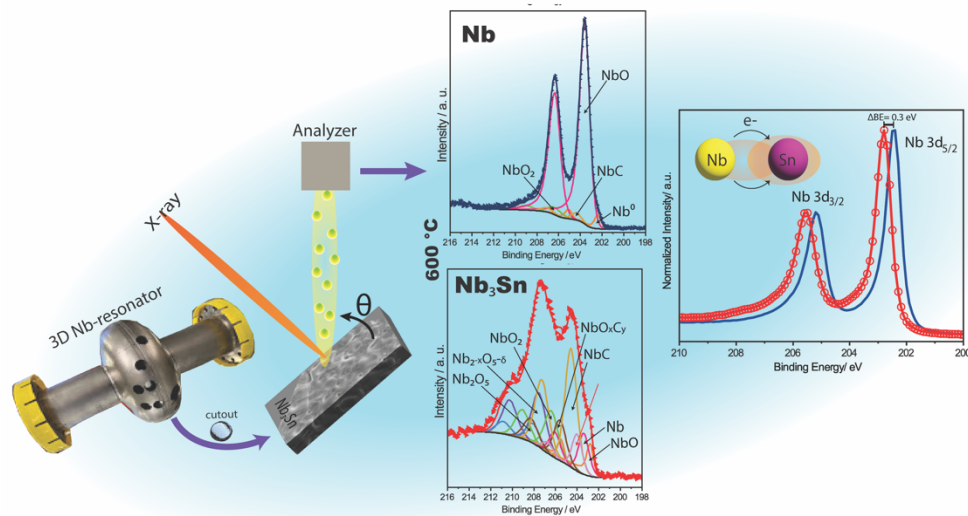
⁴SLAC National Accelerator Laboratory, Menlo Park, CA, 94025, USA

ABSTRACT

This contribution discusses the results of an *in-situ* angular XPS study on the thermal evolution of the native oxide layer on Nb₃Sn and pure Nb. XPS data were recorded with conventional spectrometers using an ALK_α X-ray source for spectra collected up to 600 °C, and a MgK_α X-rays source for temperatures above 600 °C. The effect of the thickness, composition, and thermal stability of that oxide layer is relevant to understanding of the functional properties of superconducting radiofrequency (SRF) cavities used in particle accelerators. There is consensus that oxide plays a role in the surface resistance (R_s). The focus of this study is Nb₃Sn, which is a promising material that is used in the manufacturing of superconducting radiofrequency (SRF) cavities as well as in quantum sensing, and pure Nb, which was included in the study for comparison. The thermal evolution of the oxide layer in these two materials is found to be quite different, which is ascribed to the influence of the Sn atom on the reactivity of the Nb atom in Nb₃Sn films. Nb and Sn atoms in this intermetallic solid have different electronegativity, and the Sn atom can reduce electron density around neighboring Nb atoms in the solid, thus reducing their reactivity for oxygen. This is shown in the thickness, composition, and thermal stability of the oxide layer formed on Nb₃Sn. The XPS spectra were complemented by grazing incident XRD patterns collected using the ESRF synchrotron radiation facility. The results discussed herein shed light on oxide evolution in Nb₃Sn compound and guide its processing for potential applications of the Nb₃Sn-based SRF cavities in accelerators and other superconducting devices.

HIGHLIGHTS: XPS study of native surface oxide layer in Nb₃Sn and pure Nb samples; Thermally induced changes in the surface oxide layer of Nb₃Sn and pure Nb; Phase composition of the surface oxide layer of Nb₃Sn and pure Nb from combined grazing incident XRD and XPS data; Thickness of the surface oxide layer in Nb₃Sn and pure Nb; Nature of the observed differences for the surface oxide layer in Nb₃Sn and pure Nb.

GRAPHICAL ABSTRACT



KEYWORDS. Reactivity of Nb in Nb₃Sn. XPS study of the surface oxide layer in Nb₃Sn; Features for the Nb₃Sn surface oxide layer. Thermal stability of the Nb₃Sn surface oxide layer. Changes in the Nb₃Sn oxide layer on heating.

INTRODUCTION

The small-scale accelerators using Nb₃Sn technology are in the prototyping stage thanks to world-wide advances in multi-disciplinary areas [1, 2] such as cryogenics, materials science, surface engineering, etc. Nb₃Sn is leading candidate as an alternative superconductor in RF technologies mainly due to the potential accelerating gradients of about 100 MV/m [3], twice the theoretical limit of pure Nb, and the possibility to

operate at higher cryogenic temperatures than those required for Nb. Indeed, the residual surface resistance of Nb₃Sn is particularly low, in the range of $n\Omega$ [4]. Similar values have been reported for pure Nb cavities with outstanding gradients [5, 6], and even lower values were measured in Nb cavities, that were heat treated to partially dissolve surface oxide layer. This oxide dissolution is the surface-engineering technique that reduces the residual surface resistance at low accelerating fields through the dissolution of Nb₂O₅ [7]. Several studies have found evidence that the decrease of the quality factor at low fields could be related to microwave losses in Nb₂O₅ layer [8, 9, 10]. Niobium surface oxide on polycrystalline Nb is mainly composed of amorphous Nb₂O₅ and Nb_xO_y sub-oxides, with an estimated thickness close to ~5 nm [11]. The nature and thickness of the oxide layer have been widely characterized through routine electron spectroscopies such as Auger Spectroscopy and XPS [6, 12, 13, 14, 15], and most recently using techniques with atomic resolution such as TEM and STEM [16, 17, 18]. As mentioned above, electron spectroscopies are powerful surface-specific analytical techniques useful in the study of the electronic structure of amorphous and recrystallized surface oxides. To our knowledge, the protective surface layer of Nb₃Sn remains less studied. Compared with metallic Nb, Nb atoms in Nb₃Sn, must be less reactive to the oxidation process because they are involved in a bonding interaction with the Sn atom, which is more electronegative than Nb. Such an interaction lowers electron density on the Nb atom, compared with the one for metallic Nb, and reduces reactivity for oxygen. This reduction in electronegativity of Nb could explain the slow growth of the native oxide layer on the surface of Nb₃Sn, resulting in a certain degree of the ordering for oxide phases, and higher thermal stability, which has implications for the thickness and stability of the oxide layer. In this study, we studied the surface structure, the chemical composition, and native oxide thickness together with the respective changes upon thermal treatments in under Ultra High Vacuum (UHV) conditions. Continuous XPS data recording during heating was used extract information on the surface oxide evolution. The initial experiments were carried out to evaluate the chemical composition by cross-section EDS maps, in combination with XPS spectra and oxide-layer thickness calculation from the angle variation approach (ARXPS) at room temperature. Then, *in-situ* angular XPS was used to follow the selective natural oxide layer evolution in Nb₃Sn and pure Nb in high temperatures, > 600 °C. Finally, in

the last section, we discuss the formation of NbC and the degassing of carbonaceous contaminants at sample temperatures below 300 °C.

EXPERIMENTAL SECTION

EP-Nb sample preparation: The sample labelled as EP-Nb has a pill shape (Diameter =1 cm and thickness= 3 mm). It was extracted from a 1.3 GHz SRF Nb cavity labeled as TE1AES008. The RF baseline treatment was applied to this cavity, and it is well-described elsewhere [6, 7, 19]. Each sample was carefully extracted from the cavity following the established cut-out protocol. This protocol [20] was applied to avoid sample heating and further introduction of contaminant particles.

Nb₃Sn sample preparation: From here, we are going to refer to Nb₃Sn-coated SRF grade Nb samples such as Nb₃Sn samples. Nb₃Sn coating protocol followed in this study has been previously reported elsewhere [2, 21]. In short summary, niobium surface is anodized at 30-50 V, which results in 60-100 nm growth of Nb-oxides. After the anodization process, the cavity surface color turns from shiny mirror-like gray into metallic blue, see Figure S1. The cavity and samples are then introduced to the furnace under ultra-high vacuum, 10⁻⁷ mBar for a period of 24 hours at 200 °C. After this low temperature heating to improve vacuum, the furnace is heated to 500 °C and held at this temperature for 3 hrs. The last heating step is carried out close to 1200 °C for several hours [2]. After the cooldown to room temperature, the assembled samples are removed and washed several times with manual high-rise pressure (HPR) and dried in a controlled atmosphere.

Grazing Incident X-ray Diffraction: The Grazing Incident X-ray Diffraction test was run at the BM25 Spline beam station of the European Research Synchrotron facilities (ESRF). The XRD experimental set-up is composed of a six-circle diffractometer, a 2x2 Maxipix detector and a large area CCD detector. The measurements were acquired to a maximum energy of 15 keV to avoid the Nb K α fluorescence signal (Nb: 20-25 keV) [22]. The calculated depth penetration for $\lambda= 0.826 \text{ \AA}$ and 1° degree of incidence angle is about $\sim 1 \text{ \mu m}$, using Parratt's equation [23]. The patterns were indexed with the Dicvol method in conjunction

with a crystalline phase identification using Match! software loaded with the ICSD database. The LeBail fitting and refined profile were carried through the FullProof package [24].

TEM sample preparation: Details of the surface of Nb₃Sn coating were systematically evaluated employing TEM. A thin TEM foil was prepared using a 600i Nanolab Helios focused ion-beam (FIB) and the TEM samples were thinned using a 30 kV Ga⁺ ion-beam at 87 pA. The samples were then fine-polished utilizing 5 kV Ga⁺ ions at 28 pA, to remove the damaged surface layers of the TEM foils. HR-STEM imaging was performed using an aberration-corrected JEOL ARM 200 and energy dispersive X-ray spectroscopy (EDS) mapping of Nb, Sn, O, which were collected to analyze the compositional changes in the surface oxide of Nb₃Sn coatings.

XPS measurements. The in-situ XPS measurements were carried out with a PHI 5000 VersaProbe III spectrometer from ULVAC PHI, Inc. equipped with a monochromatic Al K α beam and Ar cluster ion source (GCIS). The chosen spot size was 100 μ m; the spectra were recorded with a pass energy of 26 eV and 0.05 as the step size. The samples were measured as received and after 10 kV Ar cluster ion cleaning, which removes about 7 nm/min for organic contaminants calibrated with a PMMA film. It is estimated that when sputtering inorganics using this GCIB condition, the sputter rate is less than 1 \AA /min. The Angle-dependent XPS measurements, ARXPS, were acquired by tilting the sample, conventional approach, with emission angles, θ_e : 80°, 60°, 45°, 35°, 25°, 15° set to the normal surface.

In-situ XPS measurements: The Nb₃Sn witness sample was mounted on the support of the sample holder; on top of the sample a thin metallic sheet with an area opening was placed with fixing screws. The sample was kept into the load-lock until the vacuum pressure reached 10⁻⁶ mBar. Then, the sample was transferred to the analysis chamber, where the vacuum pressure is steady at 10⁻⁹ mBar. The sample was tilted to 34°, near the most instrumental grazing configuration. The heating rate was set at 5 °C/min. At every 100 °C, from 26 to 600 °C, the temperature was fixed and maintain for 1 hr., followed by the recording of the high-resolution core-level spectra of C 1s, O 1s, Nb 3d, Sn 3d and Sn MNN. The same workflow was applied to the EP-Nb sample. During the heating process of EP-Nb sample, a drop in the vacuum pressure to 10⁻⁴ mBar was recorded above 145 °C. Once the vacuum pressure was restored, the heating rate was set to 2

°C/min from 145 to 200 °C, and the spectra registration carried out at every 10 °C. After this critical range of temperatures, the heating rate was set back to 5 °C/min, and the spectra was recorded every 100 °C after 1 hr. at the temperature. The measurements at high-T for Nb₃Sn samples (> 600 °C) were performed in another XPS spectrometer mounted at the Spline Spanish beamline station at ESRF, France. The spectra were recorded using a non-monochromatic Mg K α source and an incident angle of 15°. The same annealing procedure was applied.

XPS data analysis. For binding energy calibration, Au 4f_{7/2}= 84.0 eV was used as a reference. The .spe (PHI Multipack) files were manually converted to ISO files using CASAXPS software [25]. This software was used for the curve-fitting of spectra recorded with Mg K α source, meanwhile the spectra recorded with monochromatic Al K α were fitted in Advantage v5.9929 from ThermoScientific Co. The backgrounds of inelastically scattered electrons were removed using the Shirley baseline model. For high-accuracy oxide thicknesses, the calculation was based on the procedure reported in the ISO 14701:2018 [26, 27]. For IMFP was calculated using the TPP2M formula contained in QUASES-IMFP-TPP2M Ver.4.1 software [28]. The information depth sampled, d_{θ} , was calculated using the equation $d_{\theta} = 3\lambda \sin(\theta)$ [29].

RESULTS AND DISCUSSION

Crystalline phase analysis and chemical composition distribution using HR-STEM/EDS

X-ray diffraction is an essential and non-destructive technique to identify the phase composition and crystallinity degree in any solid material. Specifically, Grazing-Incidence X-ray diffraction (GI-XRD) is widely applied to the study of thin films, by controlling the depth penetration into the film by incidence angle or photon energies selection. The Nb₃Sn samples under study were prepared using vapor diffusion technique with a mixture of SnCl₂ and Sn on an anodized Nb substrate; more details about sample preparation are available in the experimental section. The GI-XRD diffraction patterns for the Nb₃Sn samples were recorded with a synchrotron photon energy of 15 keV and incident angle of 1°. The diffraction peaks were indexed using the DicVol method and then verified by Le Bail profile fitting (Figure 1a). These XRD patterns reveal that the coating was successful and therefore the formed Nb₃Sn has an ordered and

regular structure. The unit cell found corresponds to a primitive cubic structure with Pm-3n space group and clearly shows a variation in the lattice parameter from 0.5308 to 0.5346 nm, probably related to a non-homogeneous local composition (discussed below). In the structure of the intermetallic material, Sn atoms are found forming a bcc sub-cell while the Nb atoms are situated on three orthogonal chains in the faces of a cube. Such chains are found parallel to the [100], [010], and [001] axes [30], Figure 1b. The Sn-Nb distance is about 2.95(9) Å and 2.64(10) Å for Nb-Nb, which is about ~7% smaller than the Nb-Nb distance in pure bcc-Nb. The high-resolution diffraction pattern reveals a mixture of fundamental peaks leading to a lattice parameter variation. The Nb₃Sn fundamental peak splitting was previously observed by Becker et al. [31], where the fundamental peaks showed a shoulder on the high angular side. In that study, the high-resolution diffraction pattern was recorded with a θ -2 θ Bragg-Brentano approach. The pattern fitting reveals two Nb_{1- δ} Sn _{δ} phases with δ =18 and 25 %, with the former phase occupying 25% of the film volume. In our diffraction patterns, at the higher angular side recorded, e.g., plane (4 2 2), the fundamental peak splits into a set of components, Inset Figure 1a. Therefore, the lattice variation (0.5308 to 0.5346 nm) may result from a deviation in the Sn concentration, 18-25 % Sn, relative to the nominal stoichiometry Nb₃Sn, which crystallizes with a cubic unit cell [32]. Such a composition deviation is consistent with the Nb₃Sn phase diagram. The presence of local defects such as vacancies also cannot be discarded. No reflections corresponding to Nb-substrate were identified in the recorded XRD pattern. This agrees with the estimated thickness, of about ~3 μ m, for the deposited Nb₃Sn film, while the calculated X-ray depth penetration in our experiment with wavelength λ = 0.826 nm and 1° degree corresponds to ~1 μ m [23]. On the surface, the interatomic spacing is different from the bulk and therefore, no lattice order is found. Indeed, the diffraction patterns do not reveal the presence of any reflections of Nb-oxides. A TEM specimen was prepared using FIB, see Experimental section. Then, high-resolution Scanning Transmission Electron microscopy (HR-STEM) experiment was conducted. The HR-STEM image shows excellent agreement with XRD results with the absence of diffraction peaks from crystalline Nb-oxides. Figure 1d illustrates the amorphous nature of the oxide layer; its thickness was roughly estimated to be about 5 \pm 1 nm. Additionally, the micrograph reveals well-resolved Nb₃Sn atomic columns, confirming the Nb₃Sn structure. A drawing

of the atomic ordering is illustrated in the Inset of Figure 1d. From the thin TEM specimen, the chemical composition was estimated with Energy Dispersive Spectroscopy (EDS) mapping. The elemental EDS maps reveal a layered distribution of Nb K, Sn L and O K, where the top surface is Sn-enriched (Figure 1c), followed by a saturated layer of Nb and O. This feature in the last spectra suggests that Nb-oxides are present on the Nb and Sn layer corresponding to Nb₃Sn. All these features agree with the HR-STEM image. Additionally, to corroborate the depth distribution observed by EDS mapping, specifically the composition of the topmost surface, complementary data were obtained by ARXPS measurements. Nb 3d, O 1s and Sn 3d spectra were recorded at four angles from 15 to 60 ° degrees, and the corresponding depth penetration was calculated (Fig. S3). All the spectra recorded were quantified using the sensitivity factors reported by Wagner and Scofield integrated in the Advantage software. As take-off angles increase, the atomic Nb:Sn ratio decreases from 2.3 to 1.9, revealing an increase of Sn at the surface. On the other hand, the Nb:O ratio increases from 0.37 to 0.45 atomic ratio as take-off angles decrease, the decrease of O to Nb ratio at deeper angles leads to the conclusion of higher near-surface O. Sn:O ratio at different angles does not show any definitive variation.

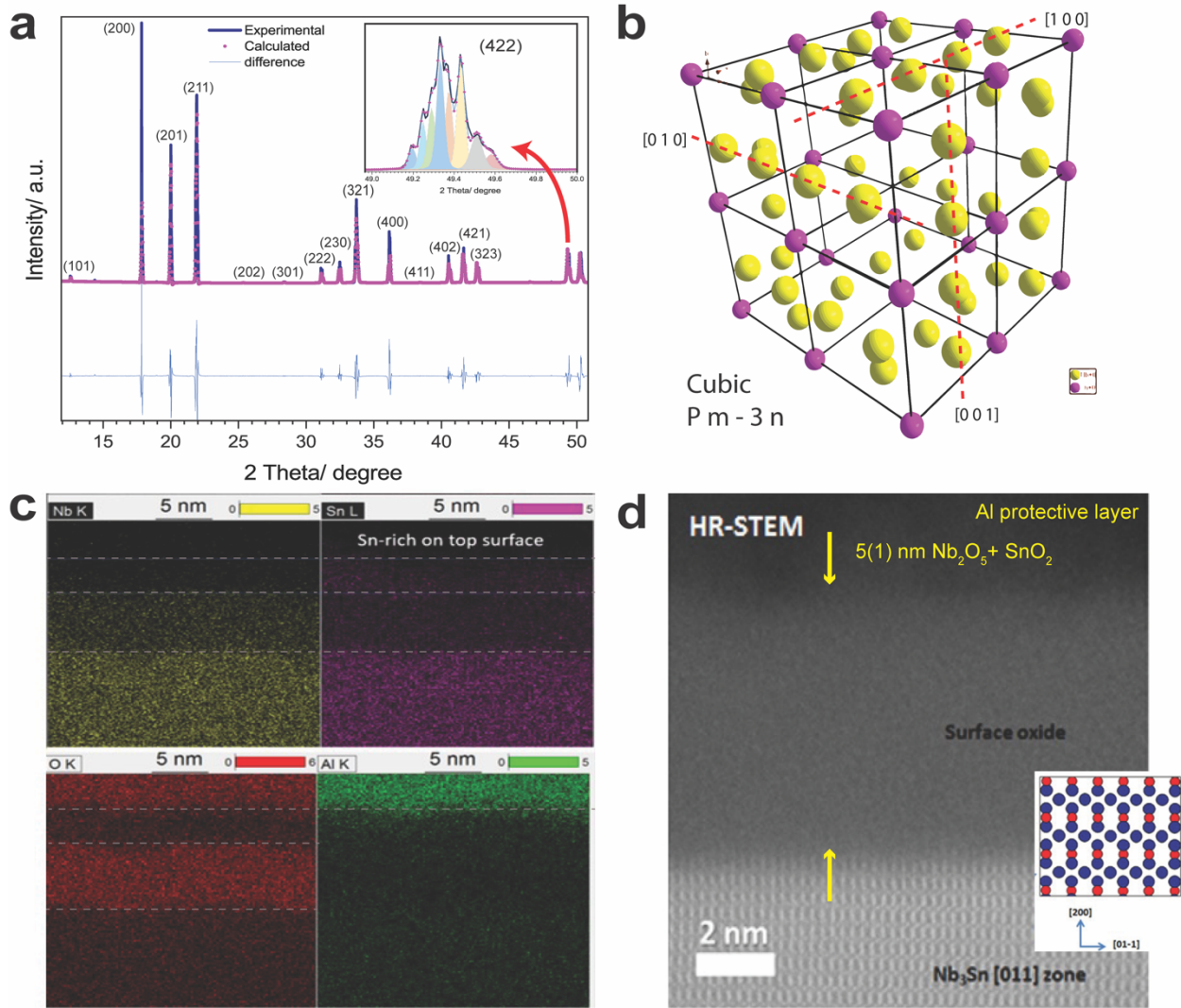


Figure 1. a) Nb_3Sn experimental and calculated XRD pattern recorded at a shallow angle of 1° , b) Atoms packing within the Nb_3Sn framework, c) Elemental composition by EDS mapping, and d) high-resolution STEM image showing the amorphous oxide layer and crystalline and well-ordered Nb_3Sn atomic structure in the $[0\ 1\ 1]$ direction. Inset: atomic model illustrating two atom sites: Nb (red) and Sn (blue).

- Estimated thickness of the oxide layer from TEM and AR-XPS data

It is important to identify oxide composition as well as the thickness of the natural oxide layer in EP-Nb and Nb_3Sn to better understand the role of the oxide layer in the low-field Q-slope [6]. Previous studies reported on the complex Nb-oxides on the surface of SRF Nb cavities after different chemical and heat

treatments [6]. Delheusy et. al. reported from their studies [33], using photon energy variation XPS, that the topmost surface layer on Nb has 2-5 nm of niobium oxides. The Nb-oxide layer consists of Nb₂O₅ on top, followed by NbO₂, NbO, and metallic Nb. Additionally, two components identified such as P1 and P2 were fitted in the proposed model. P2 component was assigned to be Nb₂O, located below NbO, meanwhile P1 was assigned Nb₂O₃, found below P2, next to metallic niobium at the metal/oxide interface. In our study to determine the layered oxide ordering in the EP-Nb and Nb₃Sn samples, we use ARXPS in an XPS lab-based instrument equipped with an AlK α source. As described in the experiment section, we use a conventional ARXPS approach [34] where the sample is tilted to a set of angles (15°, 25°, 35°, 45°, 60°, 80°) towards the energy analyzer opening. Besides, to calculate the thickness, the methodology according to ISO-14701:2018 was used [26]. The Nb 3d core-level appears as two peaks due to the spin-orbit effect. The Nb 3d curve-fitting model consists of two asymmetric peaks corresponding to metallic Nb, Nb 3d_{5/2} at 202.5 eV and the Nb 3d_{3/2} peak being at a 2.7 eV higher binding energy, with an area ratio of 3:2. Then two symmetric doublets from the Nb₂O₅ and NbO₂ oxides were fitted at 208 and 206.4 eV, with a spin-orbit difference of 2.74 eV and, each Nb 3d_{3/2} peak area being the 60 % of their Nb_{5/2} counterpart. In a row, the contribution of Nb oxide with metallic nature was added by one doublet asymmetric peaks at 203.4 eV, and binding energy difference of 2.72 eV. Considering this curve-fitting model proposed for the sample EP-Nb, the calculated thickness using the equation (S1) and (S2) is estimated at $d_{\text{Nb}_2\text{O}_5} = 4.9$ nm. The Nb-suboxides (NbO and NbO₂) are estimated with lower accuracy resulting in $d_{\text{NbO}} = 0.9$ nm. Both thickness values then give the total oxide thickness of EP-Nb, which results in $d_{\text{total}} = 5.8$ nm. The same procedure was applied to calculate the effective oxide thickness for the Nb₃Sn sample. The complex oxide layer in Nb₃Sn consists of Nb and Sn oxides. Therefore, Sn 3d spectra were considered and fitted into two contributions, two asymmetric peaks with a binding energy difference between them of 8.4 eV and an area ratio of 3:2 corresponding to metallic Sn. The second set of symmetric peaks corresponding to Sn oxides, separated by 8.4 eV, with a 3:2 area ratio. The calculated thickness from Sn oxides is $d_{\text{SnO}_2} = 1.8$ nm. The calculated thickness of niobium oxides in Nb₃Sn is $d_{\text{Nb}_2\text{O}_5} = 4.7$ nm, followed by Nb suboxides with thickness $d_{\text{NbO}} = 2.7$ nm. As we describe above, the effective oxide thickness is the calculation of all the components'

thickness ($d_{\text{Nb}_2\text{O}_5(1)} + d_{\text{Nb-sub}}$), therefore the thickness of the oxide layer in Nb_3Sn results in $d_{\text{total}} = 7.4$ nm. From the angle variation measurements, we suggest that the surface composition order is given as follows: on top, SnO_2 and Nb_2O_5 oxides are the intermixed species followed by the sub-oxides layer, and the metallic Sn and Nb components. Nb_3Sn shows a more complex surface oxide, where Nb_2O_5 layer is about 0.2 nm thinner than in pure Nb, but niobium suboxides layer is 1.8 nm thicker, Figure S3 [inset]. These findings corroborate our early argument that the electron density donation of the Nb atoms towards Sn atoms leads to a stronger bond. In addition, shorter Nb-Nb distance gives rise to a stronger metallic bond, and, therefore, Nb reactivity is diminished to form bonds with other elements such as oxygen.

-Thermal stability of Nb oxide layer in EP-Nb cutout

The native oxide layer in pure-Nb has been characterized in the previous sections by a series of analytical techniques to determine the chemical and depth composition, amorphous nature, and thickness. In summary, we found that the passive oxide layer in the EP-Nb sample consists of disordered phases of Nb_2O_5 at the topmost surface with a thickness of 4.9 nm, followed by an Nb-suboxides layer of c.a. 0.9 nm, which is mainly formed by NbO_2 and NbO phases. The removal of the native oxide layer in SRF Nb cavities enhances the quality factor Q_0 by decreasing the residual surface resistance [35]. These “oxide-free” SRF cavities undergo heat treatments above 300 °C for a couple of hours and, remain under vacuum until cryogenic RF test to avoid a re-growth of a new oxide layer in air.

In this section, we analyze the thermal stability of the passive oxide layer in the EP-Nb sample up to 600 °C. Unlike previous reports where the per-default spectrometer angle is used (commonly 45-60°), in our experiment the sample was tilted to 34° to access finer surface details by enhancing the surface sensitivity. The sample remains at this angle upon heating from room temperature to 600 °C. The progressive dissolution of the native oxide layer was followed up by recording the Nb 3d, O 1s and C 1s sub-spectra every 25 °C. At 200 °C, the Nb 3d XPS spectrum, Figure 2, is fitted with four components: Nb_2O_5 at 208.0 eV (84.5 at. %), NbO_2 at 206.4 eV (10.6 at. %), NbO at 203.4 eV (1.0 at. %), and metallic Nb at 202.5 eV (3.9 at. %). Upon heating at 225 °C, the doublet peak assigned to Nb_2O_5 becomes broader along with a

decrease in intensity. This doublet is then fitted into two phases, the original Nb₂O₅ and a new non-stoichiometric phase assigned to Nb₂O_{5-δ}. Both phases represent the 74.1 at. % of total Nb. Nb 3d peaks of the Nb₂O_{5-δ} phase are shifted 0.5 eV towards lower binding energy as compared to Nb 3d peaks for the Nb₂O₅ phase. Upon heating, Nb-O bond breakage within the amorphous Nb₂O₅ network, where Nb atoms are surrounded by oxygen atoms with electronegative character, causes the re-distribution of electron density around Nb atoms and the corresponding 0.5 eV chemical shift in the binding energy of Nb 3d electrons. Next to Nb₂O_{5-δ} peak, the contribution of NbO₂ is present at 206.4 eV with 12.1 at. % of total Nb. Metallic Nb and NbO represent the 4.7 and 1.1 at. % of total Nb. Upon heating to 325 °C, the Nb 3d spectra can be decomposed without Nb₂O₅ oxide contribution suggesting the complete dissolution of this oxide. On the other hand, Nb₂O_{5-δ} phase is reduced to 2.3 at. %, NbO₂ to 5.7 %, and most of the oxides are reduced to NbO and metallic Nb with 53.4 at. % and 9.7 at. %, respectively. At 425 °C, Nb₂O_{5-δ} phase is finally completely dissolved. The Nb 3d spectrum shows the existence of NbO₂ (206.5 eV), NbO (203.5 eV), and metallic Nb (202.5 eV) with atomic percentages of 5.5, 38.9 and 9.3 of total Nb. At 525 °C, NbO₂ is still present with 5.8 at. % at 206.5 eV as binding energy (Nb 3d_{5/2}). Metallic Nb represents the 5.4 at. % of total Nb. Then, the main composition at 525 °C is NbO with 80.4 at. %. The peak corresponding to NbO is shifted 0.3 eV towards the high binding energy side. Eventually, at 600 °C, the maximum temperature reached in this experiment, the Nb 3d spectrum is composed of metallic Nb at 202.5 eV (4.2 %), NbO at 203.7 eV (89.2%), NbC at 204.6 eV (2.8 %) and NbO₂ at 206.5 eV (3.8 %).

Besides Nb oxide evolution upon heating, Nb-C and Nb-O-C phase formation is found above 225 °C. At 225 °C the simultaneous formation of two new intermedia phases [36] is observed, corresponding to NbO_xC_y and Nb-carbides. The phase identified such as NbO_xC_y and NbC represents 6.0 and 1.8 % of total Nb, with binding energies of 205.6 and 204.5 eV, respectively. The formation of Nb-carbides [37] could be the result of the diffusion process of C into the near-surface and grain boundaries upon heating. The source of C is related to the hydrocarbons (C-H, C-C, C=C, etc.) that exists on the surface, due to air exposure and handling of samples before analysis. To confirm the presence of Nb-carbides proposed in our Nb 3d curve-fitting model, the C 1s spectra were also analyzed upon heating from room temperature to 600 °C, Figure

S7. A new peak at 283 eV along with the C adventitious at 284.6 eV is observed in the C 1s spectrum at 225 °C. This phase was monitored by the C 1s spectrum and the synthetic peak in Nb 3d at 204.4 eV showing high stability up to 600 °C. On the other hand, the intermedia phase, NbO_xC_y , exists only at 225 °C and could be the precursor for the Nb-carbides phase. The presence of Nb_2O_3 is also observed at 325 °C and 425 °C and then it is reduced to NbO. Nb 3d spectra analysis of the dissociation of the oxide layer is complemented with the O 1s spectrum curve-fitting, where the oxygen species were identified, see Figure S5.

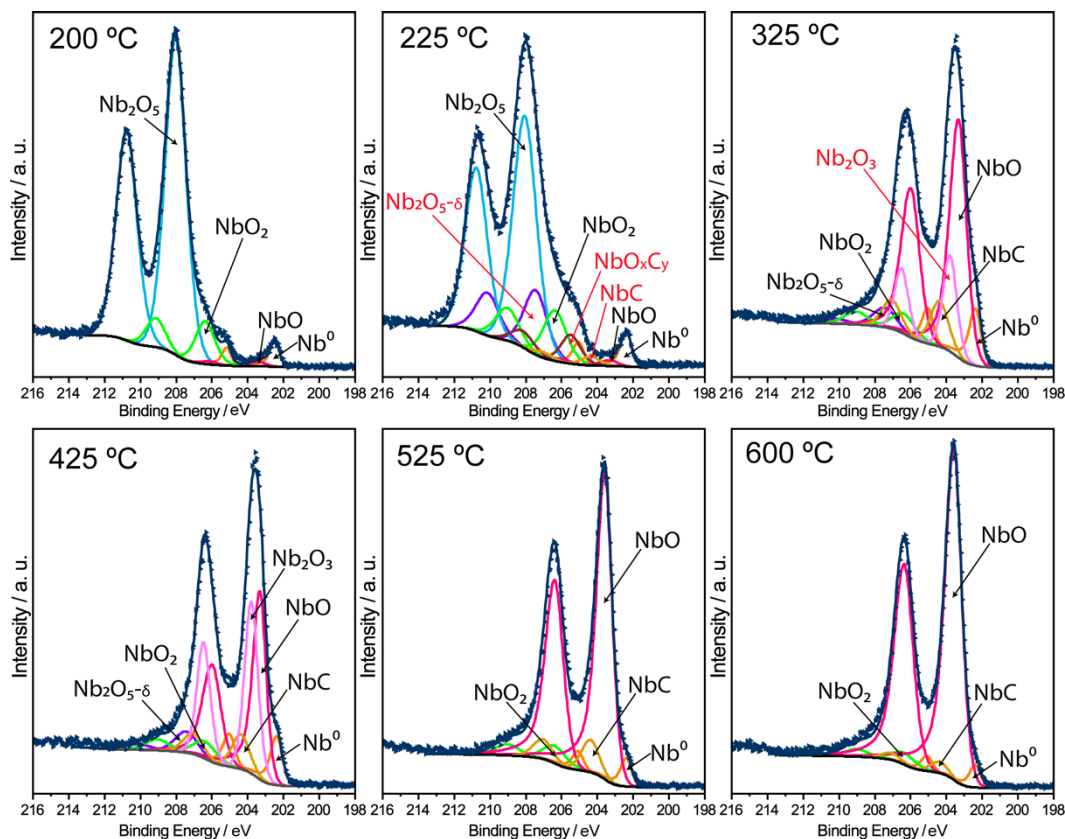


Figure 2. Nb 3d species XPS curve-fitting resulting for the EP-Nb sample upon heating to 600 °C. The EP-Nb sample was extracted from a 1.3 GHz SRF cavity, baseline-treated. Sample treatment is described elsewhere [6].

-Thermal stability of Nb_3Sn oxide layer at high temperatures (> 600 °C)

Post-coating heat treatments are the potential post-processing technique for Nb₃Sn SRF cavities to improve their performance. As mentioned above, heat treatments applied to pure-Nb SRF cavities aim to reduce residual resistance through the dissolution of the oxide layer and to improve BCS resistance through impurity diffusion. In our study, we characterized the Nb₃Sn oxide layer and its evolution upon heating by EDS mapping, HR-STEM, and ARXPS to determine the depth chemical distribution, crystalline order, and thickness. As previously discussed, the complex amorphous layer in Nb₃Sn consists of 4.7 nm of Nb₂O₅ intermixed with SnO₂ on the topmost surface and 2.7 nm of Nb-suboxides. Nb₂O₅ layer in Nb₃Sn is thinner than it is in Nb due to a lower reactivity of Nb atoms, surrounded by Sn atoms, to oxygen. We suggest that the strong overlap of the Nb and Sn electronic structure leads to a higher thermal stability of Nb₃Sn oxide layer. We have not found Nb – Sn – O phase diagram that could help us evaluate the thermal stability of Nb₃Sn oxide layer. In previous *in-situ* XPS studies performed by this group and unpublished, Nb₃Sn sample was *in-situ* heated under UHV conditions at ~300 °C for 1 h, and, unexpectedly, the peaks corresponding to Nb₂O₅ phase were still present, revealing a higher stability of Nb₂O₅ in Nb₃Sn than in pure-Nb. The Nb₂O₅ peaks are no longer observed in the Nb 3d spectrum recorded from Nb upon ~300 °C for 1 h, while in Nb₃Sn, the Nb₂O₅ peaks are dominating the spectrum. In the following section, we followed up on the evolution of the oxide layer in Nb₃Sn from 200 to 700 °C to determine the temperature of dissolution of the oxide layer as well as to identify the phases resulting from the reduction of oxide phases. This study is the first of its kind to study the nature of Nb₃Sn oxide layer along with its thermal stability in order to develop post-coating heat treatments on Nb₃Sn SRF cavities to decrease the surface resistance at low temperatures.

Sn MNN Auger complemented with Sn 3d

After discussing the intermixed composition of the oxide layer in Nb₃Sn, which consists of Nb₂O₅ and SnO₂, we will now discuss the Sn phases' evolution upon heating from room temperature to 600 °C. The poor sensitivity of the Sn 3d photoelectron signal in the identification of the oxidation states (4⁺, 2⁺ and metallic Sn⁰) of Sn is well known [38, 39]. Therefore, we complemented the analysis of Sn 3d spectra, with the analysis of the Auger signal, Sn MNN, where profile features accurately reveal the corresponding

valence [40]. At room temperature, the Sn 3d photoelectron spectrum consists of two peaks: Sn 3d_{5/2} and Sn 3d_{3/2} with an area ratio of 3:2. At 486.8 eV, a symmetric peak assigned to the SnO₂ phase is found with 91.4 atomic %. On the lower binding energy spectral region, an asymmetric peak was fitted with a binding energy of 484.5 eV and 8.6 atomic % that corresponds to metallic Sn, Figure S4 a. Upon progressive heating to 200 °C, the SnO₂ peak area decreases and the ratio changes to 2.8: 1 (Sn⁰). A progressive evolution was observed at 325 °C in the peak areas, see Figure S4 b, where 39% of Sn dioxide is reduced to metallic Sn, and therefore SnO₂ peak is observed as a small shoulder on the higher binding energy side of Sn⁰. Further heating to 425 °C, a very-weak peak just above the background appears at 486.8 eV which corresponds to 8% of total Sn meanwhile the 92% is metallic Sn (484.5 eV). The absence of any weak shoulders next to the metallic Sn peak at 525 °C indicates the complete dissolution of Sn dioxide. The Sn 3d spectra recorded at 525 and 700 °C only show an asymmetric peak at 484.5 eV (Sn 3d_{3/2}), and its Sn 3d_{5/2} spin-orbit component is 8.4 eV above. Figure S4 c shows the XAES Sn MNN lines recorded in the interval from 200 to 600 °C. In principle, the Auger spectrum at 200 °C consists of two broad peaks at kinetic energies of 425 and 433 eV. Both signals were assigned to oxidized Sn, meanwhile Sn⁰ is observed as small peaks at higher kinetic energies of 437.2 eV and 428.7. Upon heating, most oxides are reduced to metallic Sn. Therefore, the following Auger spectra from 425 to 700 °C are composed of a fine structure corresponding to two main peaks ¹G₄ and their respective multiplets, which result from the 4d⁸ final-state configuration [41]. The ¹G₄ spin-orbit splitting in our spectra with an energy difference of 8.5± 0.1 eV agrees with the literature, and therefore corroborates the complete reduction of Sn-oxides upon heating to 525 °C.

Nb 3d core-level region

Building on Sn oxide dissolution discussion, we now turn to the niobium oxide evolution in Nb₃Sn with the analysis of Nb 3d spectrum. All the spectra were taken at the shallow angle of 34 ° upon heating. Nb 3d spectrum at 200 °C consists of two doublets peaks assigned to metallic Nb at 202.8 eV (Nb 3d_{5/2}) and Nb₂O₅ at 208.1 eV (Nb 3d_{3/2}), with an area ratio between them 1:3. We applied the same curve-fitting model used for Nb 3d in the EP-Nb sample. Although in Nb₃Sn, the spectrum at 200 °C, Nb₂O₅ at 208.1 eV occupies

only 8.9 atomic % of total Nb, suggesting an early reduction of the original Nb₂O₅ into the non-stoichiometric Nb₂O_{5-δ} at 207.9 eV (50.3 at. %). The rest of the fitted phases are NbO₂ at 206.4 eV (6.6%) and NbO at 203.4 eV (6.3%) and Nb-Sn at 202.8 eV (27.9%). Upon heating to 225 °C, two new phases appear. The simultaneous reduction of NbO₂ leads to the formation of NbC_xO_y phase at 205.6 eV as well as Nb_xC_y (Nb-carbides) at 204.5 eV. The curve-fitting parameters and phase identification are available in the supplementary information file, Table S2. Upon heating to 325 °C, the spectrum profile does not show major modifications in terms of binding energy values for NbO₂, NbO, Nb⁰, NbC, Nb₂O_{5-δ} and Nb₂O₅. Nevertheless, the atomic percentage of Nb₂O_{5-δ} decreases from 50.3 at.% (200 °C) to 43.7 at. %, and simultaneously the contribution of NbO₂, NbC and NbC_xO_y increases to 7.2, 2.8, and 4.3 at. %. The continuous reduction of Nb₂O_{5-δ} progresses slowly at 425 °C. The double peaks assigned to Nb₂O_{5-δ} represents the 35.1 at. %, and Nb-Sn represents 17.1 at. % of total Nb, meanwhile the rest of Nb is shared by the phases of NbO₂, NbC and NbC_xO_y. Upon heating to 525 °C, the Nb₂O_{5-δ} phase at 207.7 eV and Nb₂O₅ phase at 208.1 eV peaks decrease in intensity and the calculated atomic percentage is 29.2 % of total Nb. Along with the reduction of Nb⁵⁺-containing phases, NbO, NbC, and NbC_xO_y increase their atomic percentage to 43.2 %. The decrease for the Nb⁵⁺ phases is reflected in a distortion of the spectral profile as observed in Figure 3, where the gap between the Nb 3d spin-orbit peaks is no longer resolved. This feature is mainly due to the increase in the NbO₂ and NbO phases. No changes in the binding energies are observed. Consequently, for the Nb 3d spectrum curve-fitting, recorded at 600 °C, the binding energy values assigned for each phase were fixed, and only the intensity was allowed to vary according to the experimental spectral profile. At this temperature, a new phase appears, and it is assigned to Nb₂O₃ at 204.0 eV which represents the 7.9 at. %. Although, all the phases are present, the total intensity of Nb₂O_{5-δ} at 207.6 eV and Nb₂O₅ at 208.1 eV decreases to 21.8 at. %. From these experiments, we find that Nb⁵⁺ phases (Nb₂O_{5-δ} and Nb₂O₅) are present even upon heating to 600 °C.

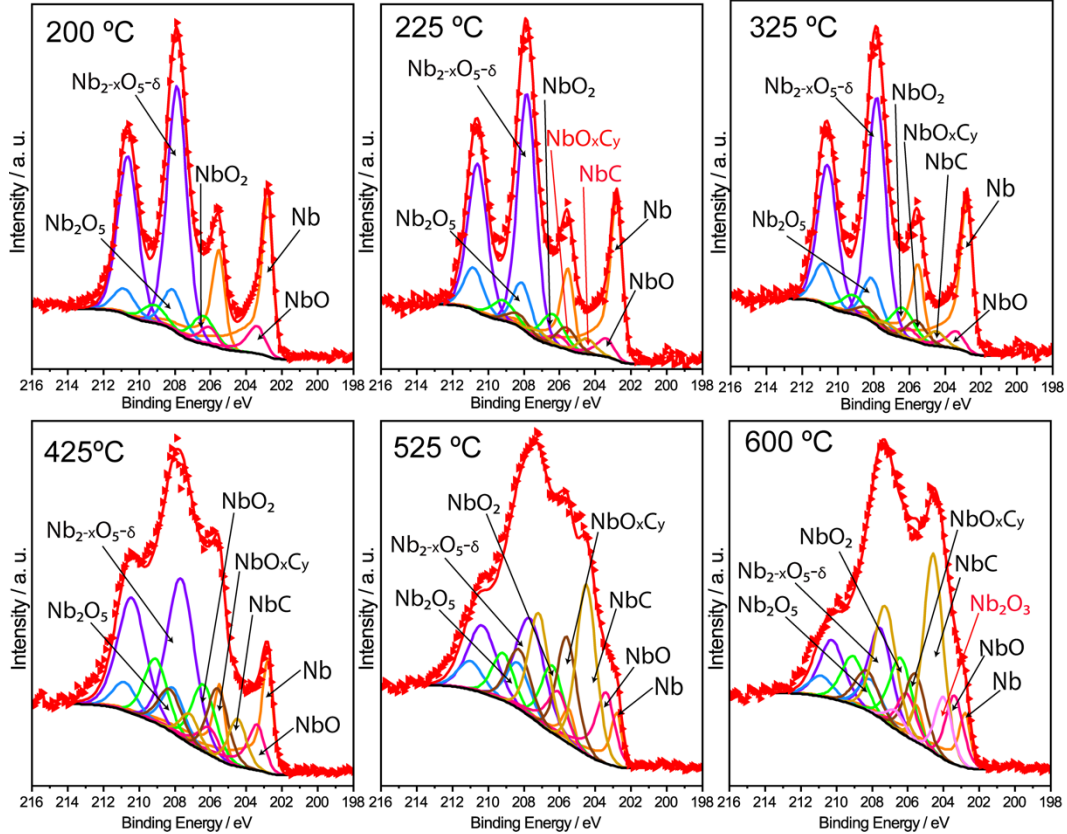


Figure 3. Nb 3d XPS curve-fitting resulting from Nb₃Sn-coated SRF grade Nb sample, clearly showing the high stability of the Nb-suboxides at 600 °C.

The next set of measurements was carried out in XPS instrument equipped with a heating stage that can reach the maximum temperature of ~1300 °C under ultra-high vacuum environment. Contrary to the previous setup, where the angle was modified at 34° for most surface sensitivity, all the spectra were recorded under the normal “bulk” angle upon heating from room temperature to 700 °C. Figure 4 shows the progressive evolution of the Nb₃Sn oxide layer with the curve-fitting of Nb 3d spectrum upon heating from 325 to 700 °C. As already discussed, the double peaks corresponding to Nb₂O₅ and Nb₂O_{5-δ} are observed at temperatures of 325 and 425 °C with an atomic percentage decrease of 68.9 to 52.3. Like the earlier experiment at 525 °C, the Nb 3d spectrum is well-fitted into the four phases assigned to NbO₂, NbC, NbC_xO_y and metallic Nb. Besides these phases, peaks corresponding to Nb₂O₅ and Nb₂O_{5-δ} were also defined with the peak intensity decreasing to 20.5 % and 1.9 %, respectively. There are differences in the spectra

recorded at 600 °C between the two experiments. In the second measurement, the Nb 3d spectrum was fitted only into six components assigned to NbO₂, NbC, NbC_xO_y, NbO and metallic Nb. Further, a very weak peak of Nb₂O_{5-δ} was observed with a binding energy at 207.7 eV. Unlike our first experiment, where both Nb⁵⁺ phases were well-fitted with a presence of 21.8 atomic percentage at 600 °C, in this new measurement, no traces of original Nb₂O₅ phase is observed. On that ground, we suggest the dissolution of the original Nb₂O₅ oxide layer occurs close to 600 °C, but the reduced Nb₂O_{5-δ} phase is still present with a concentration of 20.5 atomic % of total Nb. The difference in the results between two experiments can be explained by the shallower detecting angle used in the first experiment, which results in a more surface sensitive capture of the Nb 3d and O 1s spectra that could be hidden in the normal “bulk” measurements. Subsequently to the reduction of the Nb⁵⁺ containing phases, the spectra is composed by NbO₂ (4.6 %), NbC (5.6 %), NbC_xO_y (13.7 %), NbO (35.7 %) and Nb-Sn (36.3 %). Upon heating to 625 °C, the complete dissolution of Nb₂O_{5-δ} and NbC_xO_y takes place. The Nb 3d spectra is then composed of the remaining four phases, NbO₂ (4.5 %), NbC (13.2 %), NbO (33.3 %) and Nb-Sn (49 %). We observed that, upon heating from 655 to 700 °C, recombination of the available oxygen atoms in the near surface with Nb take place. Such a progressive process is observed as an increase in the atomic concentration of NbO accompanied by a decrease of Nb.

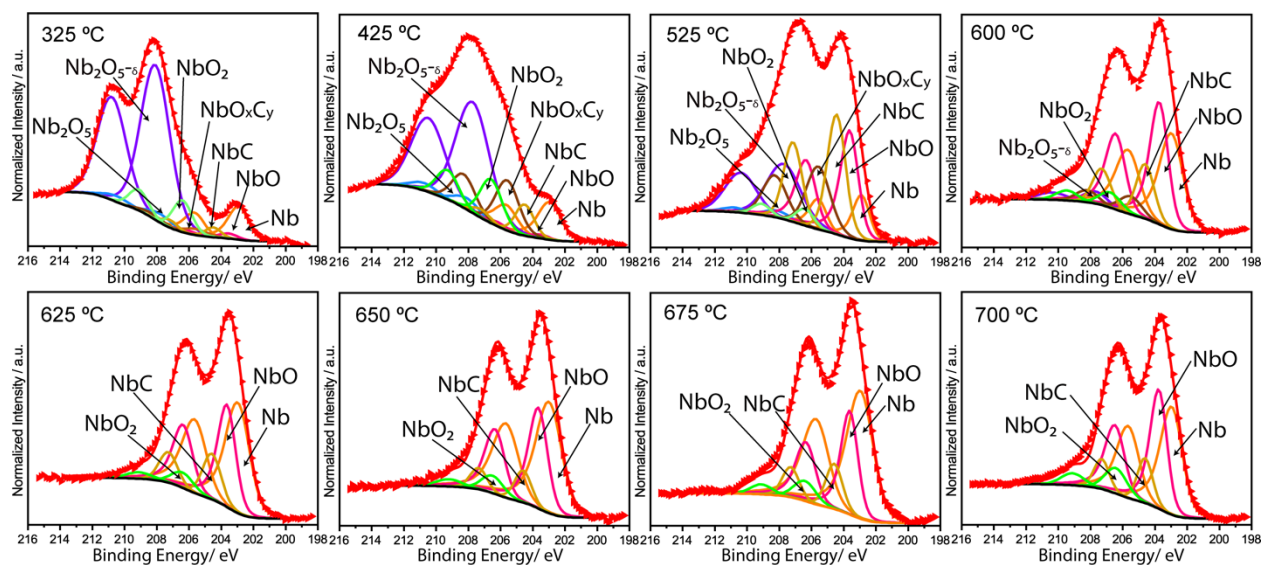


Figure 4. XPS Nb 3d curve-fitting: progressive evolution of the surface oxide layer in Nb₃Sn-coated SRF grade Nb, upon heating from 325 °C to high temperature (~700 °C).

-Carbonaceous surface-contamination removal from 145 to 200 °C

In the EP-Nb cut-out analysis upon heating, the vacuum pressure abruptly increased in the range from 145 to 200 °C. To maintain the base pressure in the analysis chamber at 10⁻⁹ mBar, we reduced the temperature ramp rate and started the spectra acquisition every 10 °C. The degassing stage, as we are going to refer to the range from 145 °C to 200 °C, was analyzed and quantified from O 1s and C 1s spectra. Figure S7 shows the decomposition of the carbonaceous phases observed as a broad shoulder at 286.2 eV. This signal disappears upon heating to 155 °C, and it is accompanied by a decrease in the atomic percentage of oxygen. This is followed by the second step in the two-step process: the evolution of the CO-contained compounds and O-contained species from 155 to 165 °C. Therefore, we could assume that the degassing stage in EP-Nb cut-out is characterized by the evolution of C and O-contained compounds, mainly located at the surface. Once overcome the critical range from 145 to 165 °C, the atomic percentage of C remains stable up to 200 °C. We suggest that a fraction of C and O atoms diffuse toward the near-surface as observed by the formation of NbO_xC_y and Nb-carbides phases from the Nb 3d and C1s spectra. Meanwhile, upon heating of Nb₃Sn sample, the vacuum pressure remained stable at 10⁻⁹ mBar up to 700 °C. We didn't register any anomaly in the critical range from 145 to 165 °C which could be related to the desorption of carbonaceous contaminants. A second measurement with an emphasis on the temperature range from 150 to 165 °C was carried out in another XPS spectrometer. Contrary to the C 1s spectra recorded from EP-Nb, the C 1s spectra recorded from Nb₃Sn consists of one symmetric peak, with no evidence of shoulders, see Figure 7 b). The vacuum pressure during this experiment remains stable at the critical temperature range, 150 to 165 °C, and no evidence of changes in the atomic percentage of C was observed. Compared to Nb metal, these experiments suggest that Nb₃Sn may have a low affinity for the absorption of carbon-based phases, and it was evident from the recorded XPS spectra upon heating below 300 °C that these phases migrate to the outer most surface region as detected and quantify in the recorded XPS spectra. Like oxygen, carbon is an

electronegative element, and a lower electron density of the Nb atom in the presence of Sn may result in a lesser affinity to the carbon-based phases absorption.

-On the nature of the thermal stability in the native oxide layer for pure Nb and Nb₃Sn

Figure 5a shows the XPS core levels of pure-Nb and Nb₃Sn samples, with emphasis on the Nb phases. Both, Nb_{5/2} and Nb_{3/2} peaks in Nb₃Sn are found to be shifted by 0.3 eV to a higher binding energy relative to the analog peaks in Nb metal. The binding energy value probes the electron density on the involved atom. An increase in the electron density results in a weaker interaction of the nuclear charge with their electrons and it is probed as a lower value for the binding energy. Inversely, when electron density is removed from the atom through an oxidation process, or when electrons are donated to other atoms during the formation of a chemical bond, the binding energy value can sense such an effect as a higher value for the binding energy. This is congruent with the dependence shows in Figure 5b for the value of the binding energy for different oxidation states of Nb [42]. In fact, the binding energy shift for Nb 3d in Nb₃Sn relative to Nb metal is a definite clue on the charge donation to the neighboring Sn atoms in the intermetallic compound. The difference corresponds to a lower electron density on the Nb atom in the intermetallic solid as the consequence of Nb atoms interaction with their Sn neighbors in the solid structure. This must be observed as a lower binding energy for Sn⁰ species, a higher electron density on the Sn atom. Such an expected shift is certainly observed as a lower value of binding energy for Sn in Nb₃Sn relative to the one observed for Sn metal (Figure 5c). This is congruent with the observed for the Sn MNN Auger region. When that region was examined for XPS spectra corresponding to metallic Sn and Nb₃Sn, the Sn MNN Auger peaks shown a definite energy shift relative to the one observed for Sn⁰, which is characteristic of a higher electron density on the tin atom in the intermetallic compound (Figure 5d). For comparison, the Auger spectral region for SnO₂ was included. In this tin oxide the tin atom has a lower electron density, and its Auger peaks appear with a pronounced shift toward to higher values of kinetic energy.

When the recorded Nb XPS sub-spectra for Nb metal and Nb₃Sn were re-examined, such a binding energy shift is observed for the considered temperature region, where the probed surface region in the intermetallic

compound remains stable. This finding supports the initial hypothesis regarding the nature for the observed differences between the surface oxide layer in Nb metal and Nb₃Sn in terms of thickness, composition, changes on heating, and thermal stability. A similar effect is expected for other Nb-containing intermetallic compounds with elements of different electronegativity, e.g., Nb-Sb, Nb-Ir (Figure 5b). The difference in electronegativity for the involved metals senses their bonding interactions and the related electron density donation/subtraction effects. The Nb and Sn 3d spectral regions shown in Figure 5a and 5c appear free of the corresponding oxide phases because the oxide layer was removed through an Argon ion beam to obtain the spectra of the naked metal surface.

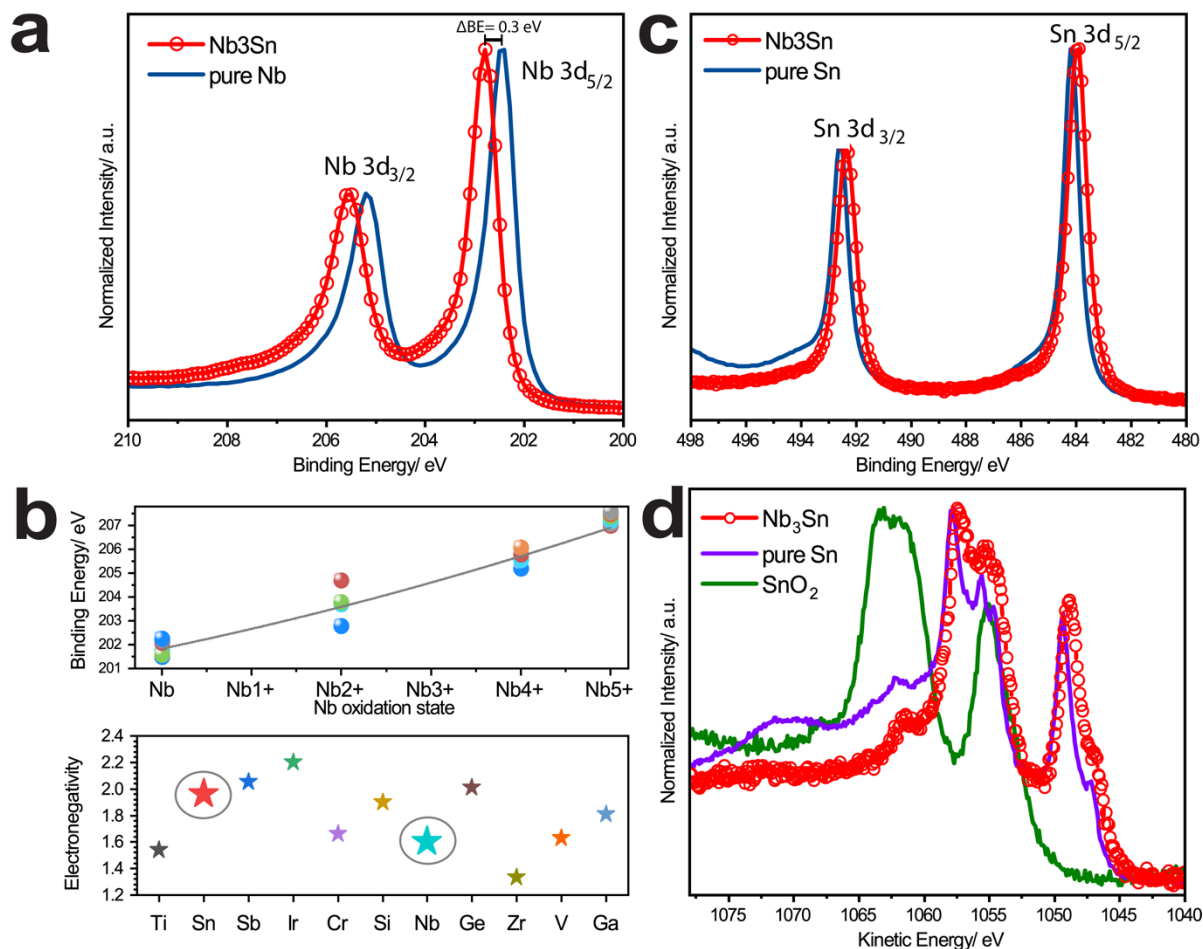


Figure 5. Chemical shift observed in the a) Nb 3d XPS spectra recorded from pure-Nb and Nb₃Sn, b) Sn 3d and d) Sn MNN feature Auger lines. On the bottom right c) represents the dependency of binding energy

respect to the density electronic in an atom, as well as the differences on electronegativities of the involved atoms in Nb₃Sn. The Nb and Sn 3d spectral regions were recorded for the surface where the oxide layer was removed through a monoatomic Ar ion sputtering at 2500 eV for 90 seconds.

CONCLUSIONS

In summary, this contribution has compared the oxide surface layer for Nb metal and Nb₃Sn in terms of the thickness, chemical and phase composition, and behavior on heating, including the thermally induced reduction processes. The surface oxide layers in these two materials show significant differences both in as-formed oxide layer and upon heating. Such differences are explained by the electronic structure of Nb atom in these two materials and its reactivity toward the oxygen atom to form oxides. The interaction of Nb with Sn in Nb₃Sn intermetallic solid involves charge donation from Nb atoms to the neighboring Sn atoms. This is effectively seen in XPS as a lower electron density on the Nb atom in Nb₃Sn relative to the value obtained for metallic Nb. The electron density is sensed through the energy shift in the core-level binding energy. Such a difference between the two materials was observed in a wide range of temperatures. These results, on the nature of the observed differences between Nb and Nb₃Sn materials, are relevant to the manufacture and processing of Nb₃Sn-based devices that operates in the superconducting state, and also guide the engineering processes towards improved performance of Nb metal-based devices, such as SRF cavities for particles accelerators and quantum computing technologies, among others.

ASSOCIATED CONTENT

Supporting information.

The Supporting Information is available free of charge on the XXXXX at DOI: XXXXXXXX

AUTHOR INFORMATION

Corresponding Authors

*E-mail: grigory@fnal.gov (G. V. Eremeev)

*E-mail: sposen@fnal.gov (S. Posen)

ORCID

Arely Cano: 0000-0003-3743-4411

Juan Rubio Zuazo: 0000-0003-0614-5334

AUTHOR CONTRIBUTIONS

A.C. and S.P. planned the research, proposed, and submitted the project; A.C. and B.L. carried out the *in-situ* XPS lab-based measurements; J-Y. L. carried out the high-resolution EDS and STEM experiments; J.R.Z. performed the high-T XPS measurements; G.E., M. M., A.R. and S.P. supervised the project. All authors interpreted and discussed the results and contributed to editing the manuscript.

COMPETING INTERESTS

The authors declare no competing interests.

ACKNOWLEDGEMENTS

This manuscript has been authored by Fermi Research Alliance, LLC under Contract No. DE-AC02-07CH11359 with the U.S. Department of Energy, Office of Science, Office of High Energy Physics. Award Number ECCS-2025124. The experimental study present herein was granted partial financial support by The Explore Nano Program from the Minnesota Nano Center. The authors are grateful to the SpLine staff for their valuable help and to the financial support from the Spanish MINECO and Consejo Superior de Investigaciones Cientificas under Grant NoMAT2011-23785, 2010 6 OE 013, ICTS-2007-02, MAT2005-25519-E, 2004 5 OE 292 andMAT2002-10806-E. A. Cano thanks to J.R. Zweibohmer for administrative and support services.

REFERENCES

1. Posen, S., Liepe, M., Ereemeev, G., Pudasaini, U. and Reece, C. E., ` Superconducting Radiofrequency Cavities: A Maturing Technology for Particle Accelerators and Detectors, *arXiv preprint arXiv:2203.06752* (2022).
2. Posen, S., Lee, J., Seidman, D., Romanenko, A., Tennis, B., Melnychuk, O. and Sergatskov, D., Advances in Nb₃Sn Superconducting Radiofrequency cavities towards first practical accelerators applications, *Supercond. Sci. Technol.* **2021**, 34, 1-10. DOI: 10.1088/1361-6668/abc7f7
3. Porter., R. D., Advancing the maximum accelerating gradient of Niobium-3 Tin Superconducting Radiofrequency Accelerator cavities: RF measurements, dynamic temperature mapping, and material growth (2021) Doctoral dissertation, Cornell University, Ithaca, NY, USA. Retrieved from <https://doi.org/10.7298/z9dj-y848>
4. Allen, L. H., Anklam, W. J., Beasley., M. R., Hammond, R. H. and Turneure, J. P., RF Surface Resistance in Nb₃Sn thin films, *IEEE Trans. Magn.* **1985**, 21, 525-527. DOI: 10.1109/TMAG.1985.1063863
5. Safa. H., High-Field Behavior of SCRF cavities, *Proceedings of 10th workshop on RF Superconductivity*, **2001**, 279-286.
6. Padamsee, H., RF Superconductivity: Science, Technology, and Applications. Wiley-VCH Verlag GmbH &Co. KGaA. (2009)
7. Posen, S., Romanenko, A., Grassellino, A., Melnychuk, O.S. and Sergatskov, D.A., Ultralow Surface Resistance via Vacuum Heat Treatment of Superconducting Radio-Frequency cavities, *Phys. Rev. Applied.* **2020**, 13, 1-10. DOI: 10.1103/PhysRevApplied.13.014024

8. Romanenko, A. and Schuster, D. I., Understanding Quality Factor Degradation in Superconducting Niobium cavities at Low Microwave Field Amplitudes, *Phys. Rev. Lett.* **2017**, 119, 1-6. DOI: 10.1103/PhysRevLett.119.264801
9. Gorgichuk, N., Junginger, T. and de Sousa R., Origin of dielectric loss at the Nb/oxide interface: Evidence for atomic two-level systems, *arXiv preprint arXiv:2203.05054* (2022)
10. Harrelson, T. F. et. al, Elucidating the local atomic and electronic structure of amorphous oxidized superconducting niobium films, *Phys. Rev. Lett.* **2021**, 119, 1-7. DOI: 10.1063/5.0069549
11. Morita, M. (1998). Native oxide films and chemical oxide films, In: Hattori, T. (eds) *Ultraclean Surface Processing of Silicon Wafer*. Springer, Berlin, Heidelberg. DOI: 10.1007/978-3-662-03535-1-42
12. Grundner, M. and Halbritter, J., XPS and AES studies on oxide growth and oxide coatings on niobium, *J. Appl. Phys.* **1980**, 51, 397- 405. DOI: 10.1063/1.327386
13. Delheusy, M. et. al, X-ray investigation of subsurface interstitial oxygen at Nb/oxide interfaces, *Appl. Phys. Lett.* **2008**, 92, 1- 3. DOI: 10.1063/1.2889474
14. Dacca, A. et. al, XPS characterization of niobium for RF cavities, *Processing of the 1997 Workshop on RF superconductivity* (1997)
15. Halbritter, J., On the oxidation and on the superconductivity of Niobium, *Appl. Phys.* **1987**, 43, 1-28. DOI: 10.1007/BF00615201

16. Tao, R., Characterization of Nb Superconducting Radio Frequency Cavities Base on In-situ STEM and EELS (2013) Doctoral dissertation, University of Illinois at Chicago, Chicago, USA.
17. Zhussupbekov, K. et. al, Oxidation of Nb(110): atomic structure of the NbO layer and its influence on further oxidation, *Sci. Rep.* **2020**, 3794, 1- 10. DOI: 10.1038/s41598-020-60508-2
18. Bose, A. et. al, Evolution of surface oxides and impurities in high vacuum heat treated Nb: A TEM and TOF-SIMS in-situ study, mechanism, and repercussions on SRF cavity applications, *Appl. Sur. Sci.* **2020**, 510, 1-12. DOI:10.1016/j.apsusc.2020.145464
19. Ereemeev, et. al., Progress with multi-cell Nb₃Sn cavity development linked with sample materials characterization, Proceeding. SRF2015
20. Romanenko, A., Surface characterization of Nb cavity sections-Understanding the high field Q-slope (2009) Doctoral dissertation, Cornell University, Ithaca, NY, USA.
21. Posen, S. and Hall, G. L., Nb₃Sn superconducting radiofrequency cavities: fabrication, results, properties, and prospects, *Supercond. Sci. Technol.* **2017**, 30, 1-17. DOI: 10.1088/1361-6668/30/3/033004 (2017)
22. Riffaud, J., Lepy, M-C., Menesguen, Y. and Novikona, A., Measurement of K fluorescence yields of niobium and rhodium using monochromatic radiation, *X-ray Spectrom.*, **2017**, 46, 341-346. DOI: 10.1002/xrs.2757
23. Parrat, L. G. Surface studies of solids by total reflection of X-rays. *Phys. Rev.* **1954**, 95, 359-369. DOI: 10.1103/PhysRev.95.359
24. Rodriguez-Carvajal, J. FullProf Suite 2013, Retrieved from <http://www.ill.eu/sites/fullprof/>.
25. Fairley, N., CASAXPS: Processing Software for XPS, AES, SIMS and More, *Casa Software Ltd., Teignmouth* (2018)

26. International Organization for Standardization, **2018**, Surface chemical analysis-X-ray photoelectron spectroscopy-measurement of silicon oxide thickness, ISO 14701:2018.
27. He, Z. et. al., Surface Investigation of Ni₈₁Fe₁₉ Thin Film: Using ARXPS for thickness estimation for oxidation layer. *Metals*, **2021**, 11, 1-9. DOI:10.3390/met11122061
28. Tougaard, S., QUASES-IMFP-TPP2M ver. 4.1, *Quases.com, Odense* (2020)
29. Schneider, T. et al., Oriented Monolayer Prepared from Lyotropic Chromonic Liquid Crystal, *Langmuir*, **2005**, 21, 23000-2307. DOI: 10.1021/la047788+
30. Van Kessel, A. T., Electronic structure and Fermi surface properties of Nb₃Sn and Nb₃Sb, Krips repro meppel, (1981)
31. Becker, C., Posen, S. and Groll, N., Analysis of Nb₃Sn surface layers for superconducting radio frequency cavity applications, *Appl. Phys. Lett.* **2015**, 106, 082602. DOI: 10.1063/1.4913617
32. Svechnikov, V. N., V. M. Pan, and Yu I. Beletskii. "Phase Diagram of the Nb—Sn System." *Physics and Metallurgy of Superconductors/Metallovedenie, Fiziko-Khimiya I Metallozipika Sverkhprovodnikov/Металловедение Физико-Химия и Металлофизика Сверхпроводников*. Springer, New York, NY, **1970**, 174-178.
33. Delheusy, M., X-ray investigation of Nb/O interfaces (2008) Doctoral dissertation, Universite Paris-sud XI UFR Scientifique D'Orsay, Paris, Fr.
34. Grant, J. T. and Briggs, D., *Surface Analysis by Auger and X-ray Photoelectron Spectroscopy*, IM Publications, (2003)
35. S. Posen, A. Romanenko, A. Grassellino, O.S. Melnychuk, and D.A. Sergatskov, Methods and systems for treatment of SRF cavities to minimize TLS losses, U. S. Provisional patent application Ser. No. 62/742, 328, *Phys. Rev. Applied* **2019**, 13, 014024

36. De Silva, V. L. S., Schmal, M. and Oyama, T., Niobium carbide synthesis from niobium oxide: study of the synthesis conditions, kinetics, and solid-state transformation mechanism, *J. Sol. State. Chem.* **1996**, 123, 168-182. DOI: 10.1006/jssc.1996.0165
37. Ereemeev, G., Study of the High Field Q-Slope Using Thermometry (2008) Doctoral dissertation, Cornell University, Ithaca, NY, USA.
38. Grutsch, P. A., Zeller, M. V. and Fehlner, T. P., Photoelectron spectroscopy of tin compounds, *Inorg. Chem.* **1973**, 12, 1431-1433. DOI:10.1021/ic50124a045
39. Felix, R., Llobera-Vila, N., Hartamm, C., Klimm, C., Hartig, M., Wilks, R. G. and Bar, M., Preparation and in-system study of SnCl₂ precursor layer; towards vacuum-based synthesis of Pb-free perovskites, *RSC. Adv.*, **2017**, 8, 67-73. DOI: 10.1039/c7ra12172e (2017)
40. Moretti, G., Auger parameter and Wagner plot in the characterization of chemical states by X-ray photoelectron spectroscopy: a review, *J. Elec. Spec.*, **1998**, 95, 95-144. DOI: 10.1016/S0368-2048(98)00249-7
41. Barlow, S. M., The M_{4,5}N_{4,5}N_{4,5} Auger spectrum of tin and oxidized tin, *J. Phys. C: Solid State Phys.* **1979**, 12, 5577-5582. DOI: 10.1088/0022-3719/12/24/029
42. NIST X-ray Photoelectron Spectroscopy Database, NIST Standard Reference Database Number 20, National Institute of Standards and Technology, Gaithersburg MD, **2000**, 20899. DOI: 10.18434/T4T88K